Available online at www.sciencedirect.com
SCIENCE DIRECT®
PERGAMON
International Journal of Heat and Mass Transfer 46 (2003) 5123–5136
International Journal of HEAT and MASS TRANSFER
www.elsevier.com/locate/ijhmt

Simulation of micro-scale interaction between ice and biological cells

L. Mao [a], H.S. Udaykumar [a,*], J.O.M. Karlsson [b]

[a] Department of Mechanical and Industrial Engineering, The University of Iowa, Iowa City, IA 52242-1527, USA
[b] Woodruff School of Mechanical Engineering, Georgia Institute of Technology, Atlanta, GA 30332-0405, USA

Received 10 May 2003; received in revised form 17 June 2003

Abstract

This paper presents numerical simulations of the response of a biological cell during freezing. The cell is modeled as an aqueous salt solution surrounded by a semi-permeable membrane. The concentration and temperature fields both inside and outside a single cell are computed taking into account heat transfer, mass diffusion, membrane transport, and evolution of the solidification front. The external ice front is computed for both stable and unstable growth modes. It is shown that for the particular geometry chosen in this study, the instabilities on the front and the diffusional transport have only modest effects on the cell response. For the cooling conditions, solute and cell property parameters used, the low Peclet regime applies. The computational results are therefore validated against the conventional membrane-limited transport (Mazur) model. Good agreement of the simulation results with the Mazur model are obtained for a wide range of cooling rates and membrane permeabilities. A spatially non-isothermal situation is also considered and shown to yield significant differences in the cell response in comparison to the isothermal case.

1. Introduction

Successful freezing of biological material for long-term storage hinges critically on the physics of interaction of ice with living matter (cells and tissue). A primary concern in cryopreservation is the damage caused to individual cells in the tissue as a result of solidification of water. While there is some debate on the details [1–4], the fundamental principles of ice-induced cell damage are fairly well understood and are summarized below. Ice formation is kinetically favored to occur first in the extracellular solution in preference to the confined intracellular space. As ice approaches a cell, solutes (e.g. salts such as NaCl) are rejected into the unfrozen extracellular solution. The increasingly salty extracellular environment results in osmotic non-equilibrium across the cell membrane. The cell overcomes this in one of two ways: (a) intracellular water is transported to the extracellular solution; or (b) ice forms within the cell, thus adjusting the osmolality inside the cell. The dominant mechanism depends on the cooling rate. At low cooling rates, water has ample time to escape from the cell, causing significant cell dehydration and preventing ice formation. However, too low a cooling rate can be detrimental to survival because the cell finds itself immersed in a progressively hypertonic environment for longer times (resulting in death due to "solution effects" [2]). Also, excessive shrinkage during slow freezing and rapid volume recovery upon thaw is believed to structurally damage the cell [5,6]. For high cooling rates, water is unable to escape rapidly enough, resulting in water being trapped within the cell. The trapping of water is exacerbated by the decrease in cell membrane permeability [7] and decrease in the mobility of water molecules as the temperature is lowered. Therefore, as the temperature drops, the intracellular solution is supercooled and the trapped water freezes, leading to intracellular ice formation (IIF) [8,9]. Cell death due to IIF is thought to occur due to irreversible physicochemical damage to the cell organelles

* Corresponding author. Tel.: +1-319-384-0832; fax: +1-319-335-5669.
E-mail address: ush@icaen.uiowa.edu (H.S. Udaykumar).

0017-9310/$ - see front matter © 2003 Elsevier Ltd. All rights reserved.
doi:10.1016/S0017-9310(03)00364-8

and membrane. Thus, there is an intermediate optimal cooling rate for cell survival and its identification is a matter of primary concern for successful cryopreservation.

Experimental observations demonstrate that the presence of extracellular ice significantly increases the probability of IIF [8]. Such observations have been explained by the hypothesis that intracellular ice forms by a nucleation process, and that interactions between the cell membrane and extracellular ice crystals create catalytic sites for ice nucleation on the interior surface of the cell [10], a mechanism known as surface-catalyzed nucleation (SCN). In order to rigorously test this hypothesis, and to elucidate the biophysical mechanisms underlying the SCN process, a detailed model of the interactions between cells and external ice crystals is required. Most modeling work on ice–cell interaction to date has resorted to a quasi-steady treatment of solute transport and extracellular ice formation, essentially following the early work of Mazur [7]. For example, solute polarization within and outside the cell is usually ignored and the cell is treated as immersed in an isothermal medium. The intra- and extracellular solutions are assumed homogeneous in composition and the extracellular ice front is assumed to be planar, and in equilibrium with the solution. The temperature and solute at the ice–solution interface are therefore related through equations that assume thermodynamic equilibrium (which ignores effects of supercooling [1]). The exception was the early work of Levin et al. [11,12], which modeled diffusion in one-dimensional cells with moving semi-permeable membranes. They showed that in the range of cooling rates where IIF occurs, both transmembrane and intracellular solute transport are important. However, even in that work, extracellular solute segregation was ignored. Significantly, in later work solute polarization was altogether neglected by Levin [13]. This is perhaps because of the considerable complexity of the higher-dimensional coupled heat and mass transport and moving boundary problem involved in ice–cell interaction. Only in the past decade or so have numerical methods become capable of tackling the complex moving boundary problem of solidification-front motion in pure [14,15] and impure systems [16]. In recent papers Jaeger and coworkers [17,18] have performed numerical simulations of the two-dimensional cell interactions with planar as well as non-planar freezing fronts and examined the thermosolutal field during the engulfment of the cells by the ice front. The present work is concerned with the shrinkage of a cell that is surrounded by an advancing ice front. The detailed long-time development of dendritic ice crystals is not simulated in the present work. The history of the ice front advance towards the cell can be important [17], but is an issue that will not be examined in the present work. However, the model developed in the present paper does afford the ability to examine the relative importance of various transport mechanisms that influence cell volumetric response to ice. These include: (a) diffusional transport of water in the extra- and intracellular solutions, (b) transport of water across the semi-permeable cell membrane, controlled by the membrane permeability, (c) ice front morphology (i.e. length scales in the case of an unstable front) and its influence on cell response, (d) salt rejection and formation of salt boundary layer ahead of the front and its influence on the cell shrinkage and (e) the coupled transport of heat and species in the non-isothermal case and the resulting differences from the isothermal case.

2. Formulation and numerical method

In this paper we use a sharp interface method [14–16] to simulate the dynamics of the phase boundary. We solve, using methods described in previous papers [16], the diffusion equations for species and temperature field in the extracellular and intracellular medium:

$$\frac{\partial c_{\mathrm{NaCl}}}{\partial t} = D_{\mathrm{l/s}} \nabla^2 c_{\mathrm{NaCl}} \tag{1}$$

and

$$\frac{\partial T}{\partial t} = \alpha_{\mathrm{l/s}} \nabla^2 T \tag{2}$$

where c_{NaCl} is the concentration of salt, T is the temperature, t is time, α and D are thermal and solutal diffusivities respectively, and subscripts l and s imply liquid and solid phases. Note that in reality the solute diffusivity is dependent on the concentration, which can vary quite markedly in the solution. Spatial variations in diffusion coefficients can be handled easily by the present numerical method. However, such variations may obfuscate other transport effects that form the central issue of investigation in this paper and this aspect is therefore left for future work.

The temperature and concentration fields are coupled through boundary conditions at the ice–solution interface, where the phase diagram relates the interface temperature and composition. The phase diagram is modeled with an empirical relationship [19]. After including capillarity effects the interface temperature is given by:

$$T_{\mathrm{Li}} = b_0 + b_1 c_{\mathrm{Li}} + b_2 c_{\mathrm{Li}}^2 + b_3 c_{\mathrm{Li}}^3 + b_4 c_{\mathrm{Li}}^4 - \frac{\gamma_{\mathrm{sl}}(\theta)}{L} T_{\mathrm{m}} \kappa \tag{3}$$

where c is the salt concentration, subscript Li indicates the interface value on the liquid side, T_{m} is the melting point of ice, κ is the interfacial curvature, L is the latent heat of fusion, θ is the angle that the normal to the interface makes with the horizontal, and the anisotropic

surface tension is modeled in the form employed in crystal growth simulations [20], i.e. $\gamma_{sl}(\theta) = \gamma_0(1\text{–}15\varepsilon\cos(m\theta))$, where ε is the anisotropy strength and m defines the symmetry characteristics. For the present simulations we adopt $\varepsilon = 0.05$ and $m = 6$ and the surface tension parameter $\gamma_0 = 0.033$ N/m for the ice–water interface, unless otherwise stated. The terms containing the constants b_i ($i = 0$–4) in Eq. (3) arise from the relationship on the liquidus curve between the temperature and concentration of species. In this work, we use only the first-order concentration-dependent term on the right hand side of Eq. (3), i.e. the liquidus curve is linearized. The species and heat balances at the ice–solution interface are given by:

$$(1-p)\cdot c_{Li}\cdot V_N = D_s\cdot\left(\frac{\partial c_{NaCl}}{\partial n}\right)_s - D_l\cdot\left(\frac{\partial c_{NaCl}}{\partial n}\right)_l \tag{4}$$

and

$$L\cdot V_N = k_s\cdot\left(\frac{\partial T}{\partial n}\right)_s - k_l\cdot\left(\frac{\partial T}{\partial n}\right)_l \tag{5}$$

where p is the partition coefficient, V_N is the normal velocity of advance of the ice front, n is the normal direction and k_s and k_l are thermal conductivities of the solid and liquid respectively. The thermal conductivity of the liquid phase is related to the concentration of salt in the aqueous solution and decreases with increasing salt solution. The value for the unfrozen liquid and for the ice is listed in Appendix A. The conductivity for pure liquid water is 0.61 W/m K. The variation of the liquid conductivity with the concentration field can be modeled by taking a linear variation with respect to the concentration from the known values at $c_{NaCl} = 0$ and at the initial concentration of $c_{NaCl} = c_0$.

At the cell membrane, which is the boundary that separates the intra- and extracellular regions, the species balances on the intra- and extracellular sides read:

$$\begin{aligned} D_{NaCl,e}\left(\frac{\partial c_{NaCl}}{\partial n}\right)_e &= c_{NaCl,e}J_w,\\ D_{NaCl,i}\left(\frac{\partial c_{NaCl}}{\partial n}\right)_i &= c_{NaCl,i}J_w \end{aligned} \tag{6}$$

where subscripts e and i apply to the extra- and intracellular medium respectively.

The flux of water from the cell due to osmosis is given by Darcy's law:

$$J_w = RTL_p(c_{NaCl,e} - c_{NaCl,i}) \tag{7}$$

In the above, L_p is the hydraulic conductivity of the membrane. The cell membrane permits water to traverse across the membrane but does not permit exchange of salts. The hydraulic conductivity decreases with temperature, and its temperature-dependence has an Arrhenius form $L_p = L_{pg}\exp(-E_a(1/T - 1/T_g)/R)$ where E_a is an activation energy for water transport, R is the universal gas constant, T_g is a reference temperature, and L_{pg} is the hydraulic conductivity at T_g. However, to clearly delineate the effects of diffusion from other effects, we set $E_a = 0$ for all the cases presented in this paper. The material parameters used in the above model pertaining to the freezing of a binary NaCl–H_2O solution were obtained from the literature [20]. The modeled cell corresponds to an erythrocyte [17]. The non-dimensional quantities and material parameters used in this work are listed in Appendix A.

3. Modeling of the response of the cell

In [16], the micro-scale freezing processes of aqueous solutions typically used in cryopreservation were simulated using the species and heat transport in the solution (Eqs. (1) and (2)). The solute and temperature fields in the solid and liquid were matched at the sharp phase boundary using the interfacial species and heat balance, Eqs. (4) and (5). The phase diagram, represented by Eq. (3) was used to relate the interfacial temperature with the species concentration. Since the interface is treated as a sharp entity in the numerical method [16] used in this work, the material property jumps, such as species diffusivity, thermal diffusivity and the partition coefficient for solute are accurately incorporated. This methodology for the computation of solidification of aqueous solutions is coupled with the heat and mass transport around a single cell. The cell is modeled as comprising a salt solution enclosed within a semi-permeable membrane. Initially, the cell rests in an isotonic salt solution. As seen from Eq. (7), the flux of water to and from the cell is controlled by the membrane permeability and is driven by the concentration differential across the membrane. The implementation of the osmotic flux across the membrane is achieved using the sharp-interface method [14]. Heat and mass transport are solved in the extra- and intracellular domains subject to the interface conditions applicable at the embedded solid–liquid (ice) front and at the cell membrane.

For purposes of comparison with the present model, a conventional membrane-limited transport model was also implemented. Eq. (7) was used to determine the rate of water transport from the cell, assuming well-mixed intracellular and extracellular compartments, and that the extracellular solution maintains an equilibrium with a planar ice front. Thus, the external salt concentration was computed using the liquidus model (based on Eq. (3)): $c_{NaCl,e} = (T - b_0)/b_1$. The salt concentration in the cell interior is given by $c_{NaCl,i} = (c_0V_0)/V$, where c_0 and V_0 are the salt concentration and cell volume, respectively, under isotonic conditions. The cell volume at each instant was determined by solving the ordinary differential equation

$$\frac{dV}{dt} = -S \cdot J_w \tag{8}$$

using a fourth-order Runge-Kutta scheme with step size control. The cell membrane surface area S was computed from the cell volume by making the conventional assumption that the cell shape remains circular during dehydration, and the temperature history $T(t)$ was defined by the given cooling protocol, assuming instantaneous heat transfer throughout the system.

4. Results

4.1. Computational setup

The computations of the freeze-front interaction with the modeled cell were performed in the configuration shown in Fig. 1. The computational domain of dimensions $10R_{cell}$ on each side was chosen where R_{cell} is the radius of the cell. The cell was placed in the center of the domain. The solid–liquid interface is initially circular and is placed concentric with the cell so that the freeze front radius is $4R_{cell}$. In the following, both isothermal and non-isothermal cases have been computed. In the isothermal case, a condition closely approximating the bulk of experiments performed on cell suspensions using cryomicroscopy, the temperature of a small sample is lowered at a specified cooling rate. The thermal diffusivity being larger than mass diffusivity, the temperature is typically considered to be uniform in the entire computational domain. The heat equation is therefore not solved in this case and the temperature field is specified everywhere (i.e. at each grid point). For the non-isothermal case, the temperature at the edge of the domain is specified based on the cooling rate and the heat diffusion equation (Eq. (2)) is solved. The interface temperature is then just the imposed temperature based on the cooling rate and the interface advection is performed by iterating to satisfy Eqs. (3)–(5) simultaneously [16]. The initial conditions for temperature and salt concentrations are specified, $T(x,y,t=0) = T_0$ is given for each case in the results section, while the initial concentration $c_0 = 0.1548$ mol/l for all cases. The boundary conditions on the domain boundaries are specified as: $T = T_0 - Bt$, and $\frac{\partial c_{NaCl}}{\partial n} = 0$.

The present numerical method has been validated [15] against solvability theory for wavelength and dendrite tip velocity selection for pure materials. As shown in Udaykumar and Mao [16], the extent of the supercooled region ahead of the ice front depends on the cooling rate. Thus, as the cooling rate increases the severity of the supercooling increases and the interface instability is enhanced. In fact, breakdown of the front into cellular/dendritic structures is inevitable for the freezing conditions adopted in typical cryoprotocols,

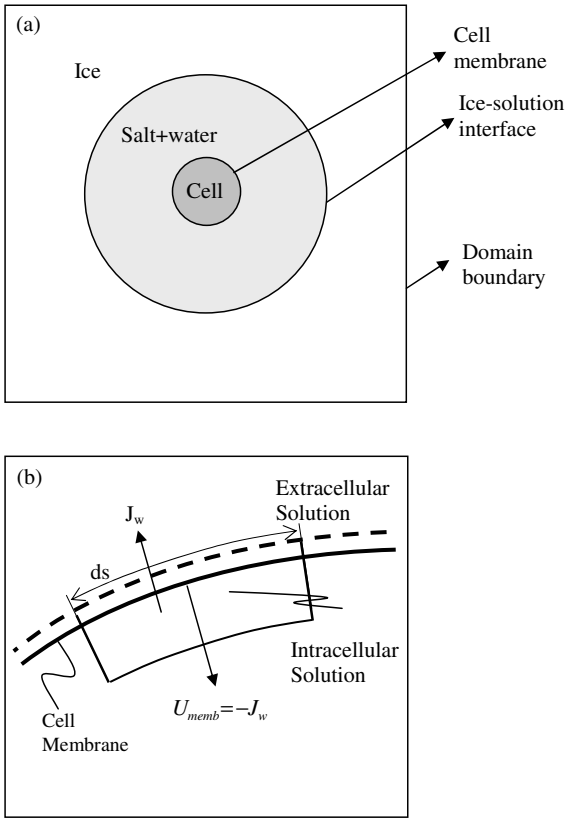

Fig. 1. Schematic of the computational model for the ice–cell interaction problem. (a) The cell and ice–solution interface are placed on a uniform Cartesian mesh and the interfaces are moved over the mesh. A finite volume discretization of the governing equations is performed on the fixed mesh. (b) The computational model for cell membrane.

even for the lowest cooling rates (1 °C/min). In the numerical simulations presented in this work the instabilities on the front arise due to numerical noise, just as in a laboratory sample the instabilities are triggered by various noise sources including environmental and thermal fluctuations. However, numerical noise (which is anisotropic due to such factors as sweep directions in the equation solver, arc length parameterization and derivative estimations on the interface etc.) leads to the development of asymmetric perturbations and the instabilities develop very slowly. To control and hasten the growth of instabilities small sinusoidal perturbations (with amplitudes of a few mesh spacings and wavelengths corresponding to 1/5th the circumference of the initial circular front) were initially superposed on the circular interface. The perturbations that grow and the wavelengths that are established in the later stages of growth are dependent on the interfacial tension value as indicated by microscopic solvability theory. In the case of high growth rate of the instabilities, for example for

large driving forces (supercooling, cooling rate) and low stabilization (i.e. low surface tensions) asymmetries in the numerically obtained fronts may arise due to the amplification of grid-induced noise. Such asymmetries can be suppressed by employing higher mesh resolutions. The computational cost to fully suppress all such asymmetries using a fine mesh may be prohibitive, depending on the growth conditions. Thus a compromise is often necessary between the computational cost and elimination of noise effects. In this work, we show that the conclusions reached on the cell response to the approaching ice front morphology are independent of occasional grid-induced perturbations that are evident on the unstable freeze front.

4.2. Cell–ice interactions

In order to assess the effect of the ice-front morphology on the cell volume response we first computed cases with artificially enhanced surface tension to suppress the development of any instability that may arise, even in the presence of the initially imposed perturbations. The surface tension in this case ($\gamma_0 = 1.65$ N/m) is therefore made high enough that the grid-scale perturbations will not grow. As we show later, this artifice has only a modest effect on the conclusions regarding cell response in the present configuration. In Fig. 2, we show results of calculations of the interaction of such a stabilized ice front with a cell. Unless specified otherwise, the following cases are isothermal. The temperature at each point in the domain decreases at the specified constant cooling rate denoted B. The cooling rates imposed in this study fall within the range of those commonly employed in cryopreservation protocols for red blood cells (100–10,000 °C/min). In the case shown in Fig. 2, the cooling rate is 1000 °C/min. In Fig. 2(a)–(d) we show the contours of salt concentration in the unfrozen solution as the ice forms, removing water from the suspending medium and causing the cell to respond by osmotic shrinkage. The boundary layer of salt accompanying the ice front is evident in the figure. The time (in seconds) corresponding to each of the figures is noted in the accompanying caption. The temperatures at the instants shown are also indicated. Note that the freezing and cell shrinkage takes place rapidly (in about 0.75 s) for this cooling rate. The temperature is only about −13 °C at the final stage in Fig. 2(d). This rapid dehydration, before the temperature falls to values close to the SCN range suggests that the protocol shown in Fig. 2 will perhaps be successful in avoiding IIF. In Fig. 2(e) and (f) we show the solute concentration profile across the domain on the horizontal centerline. The profile in Fig. 2(e) corresponds to the instant in Fig. 2(a) and that in Fig. 2(f) corresponds to Fig. 2(c). The solute partition at the ice front is clearly seen. The solute boundary layer is quite steep in Fig. 2(e) and there is a jump in the concentration at the cell membrane, which is captured well by the present sharp interface method. It is this jump that provides the driving force for water loss from the cell. In the absence of a sharp-interface treatment of the cell membrane this jump will be smeared and the correct cell shrinkage response will not be obtained. As seen in Fig. 2(f), although the solute concentration is very high at the ice front and the jump in solute concentration across the cell membrane is large, the concentrations within the extra- and intracellular solutions are nearly uniform. This is because of the low Peclet numbers in this temperature range, which makes for very rapid solute diffusion.

To establish the validity of the calculations presented in this paper, we performed several tests, which are summarized in Figs. 3–5. To demonstrate that the conclusions reached in this work are independent of the grid density employed in the simulations, the cell volume response for a case with a high cooling rate, $B = 10{,}000$ °C/min, was computed on meshes with 250×250 (Fig. 4) and 500×500 (Fig. 5) grid points. Initial sinusoidal perturbations were imposed on a circular front, with magnitude of a few mesh cells and wavelengths corresponding to 1/5th of the circumference. A comparison between the volume response on the two meshes (Fig. 3(a)) shows that the results are in close agreement. The details of the freezing front morphology and the solute concentration field are shown in Fig. 4 (for the coarser 250×250 mesh) and in Fig. 5 (for the finer 500×500 mesh). It may be noticed that the interface morphology for the coarser mesh shows asymmetries in the breakdown of the front into instabilities. This is due to the fact the lower resolution provided by the 250×250 mesh results in higher numerical noise which is amplified as the instability grows. While this spurious instability exists in Fig. 4(b) it is no longer observed in Fig. 4(c). This is due to the surface-tension-induced coarsening of the interface morphology as the front readjusts the instability wavelengths. Note that in Fig. 5, i.e. for the finer mesh, the asymmetry in the breakdown is absent throughout. Therefore, with a sufficiently fine mesh for a particular freezing protocol, the numerically induced asymmetric perturbations can be eliminated entirely. However, this comes at the expense of an increase in computational times. On the other hand, the presence of the asymmetric perturbations (superposed on the primary instabilities of the front) has little effect on the volume response of the cell as seen from Fig. 3(a). Figs. 4(d) and 5(d) reveal that the solute concentration fields for the two meshes do reflect the presence of the instabilities on the front. However, the average concentration of solute in the unfrozen solution and the resulting volume response shown in Fig. 3 is nearly identical for the two meshes. In light of our interest in the volume response of the cell and the good agreement between the results on the two meshes shown in Fig. 3,

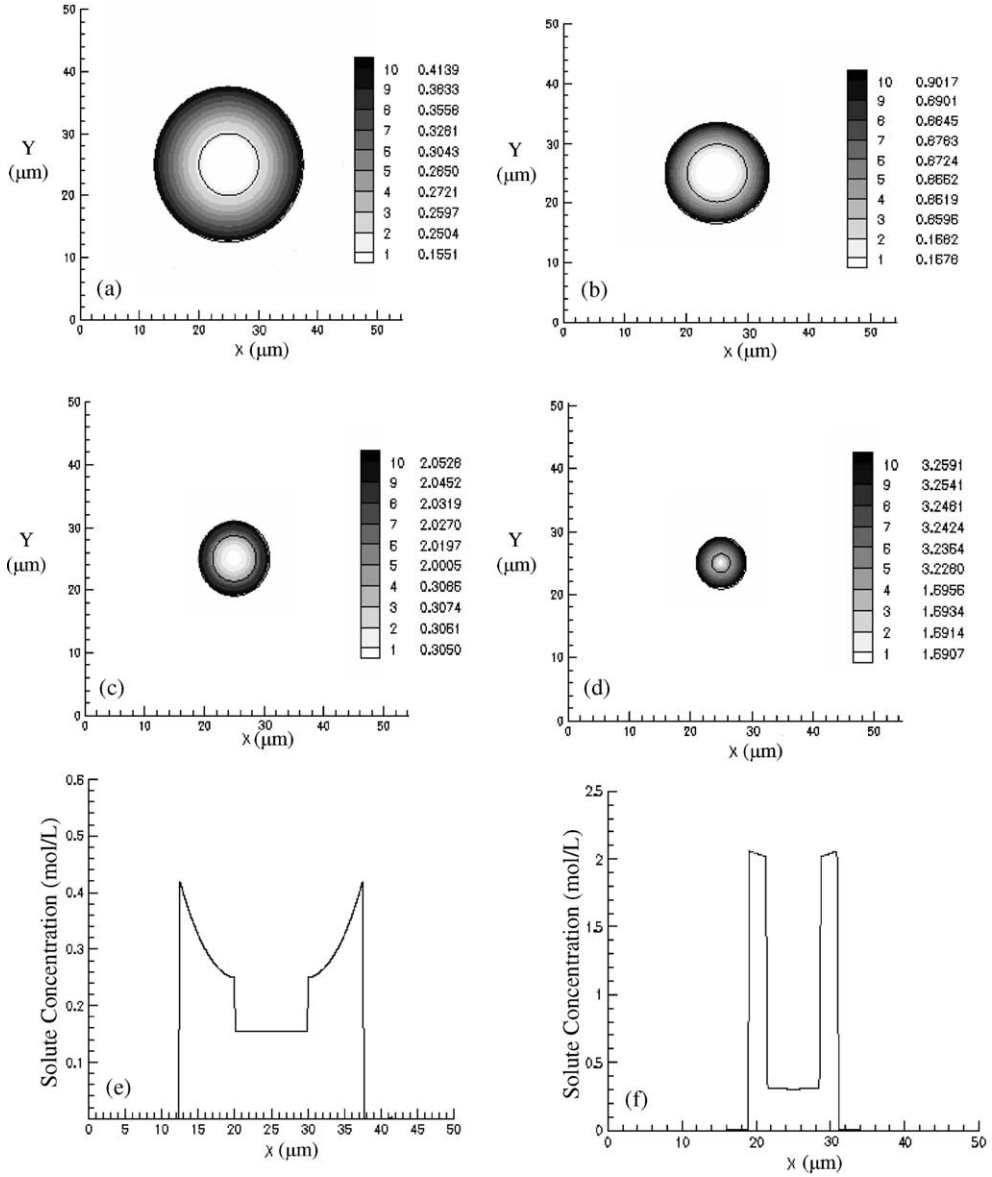

Fig. 2. Solute concentration (in mol/l) contours (indicated using gray-scales) during ice–cell interaction at the cooling rate $B = 1000$ °C/min and $T_0 = -0.54$ °C and using a high surface tension ($\gamma_0 = 1.65$ N/m) to suppress instabilities. (a) Time: 0.0526 s, temp: −1.4231 °C; (b) time: 0.1533 s, temp: −3.098 °C; (c) time: 0.4144 s, temp: −7.4476 °C; (d) time: 0.7370 s, temp: −12.819 °C. Solute concentration profiles across the horizontal centerline of the cell for: (e) time: 0.0526 s, temp: −1.4231 °C; (f) time: 0.4144 s, temp: −7.4476 °C.

we retain the 250×250 mesh for subsequent calculations.

Since the cell is impermeable to salts and only water enters or leaves the cell, the total amount of salt in the cell should remain constant as the cell shrinks. Fig. 3(b) shows the variation in the total amount of the salt in the cell with time. The ratio of the total salt contained in the cell at any time to the initial salt content (cV/c_0V_0) was computed, where subscript "0" indicates initial values. The figure shows that the total amount of salt in the cell remains close to the original value. There is a slight deviation from the expected value of 1.0 as the cell shrinks due to the fact that, as the cell shrinks, the number of grid points inside the cell decreases and hence the resolution of the intracellular medium is not constant as time progresses. Furthermore, as the cell shrinks the concentration values in the cell increase dramatically and the deviations from the solute conservation in the

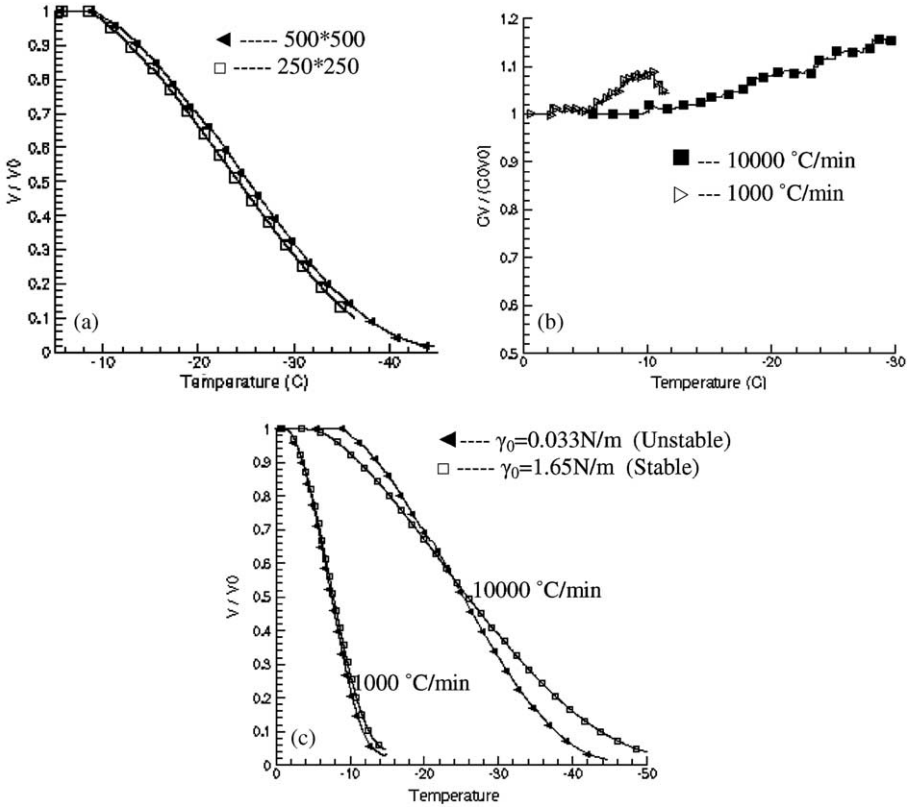

Fig. 3. The characteristics of the volume response of a cell under the influence of external ice formation studied by varying control parameters. (a) The effect of mesh size on the predicted cell volume for a cooling rate of 10,000 °C/min. (b) The total salt content in the cell plotted against temperature (equivalently time) for two cooling rates. (c) The effect of interface stability for fixed surface tension on the volume shrinkage.

cell are also inflated to some extent by these large values of concentration. This deviation can of course again be reduced by using finer meshes.

In Fig. 3(c) we assess the effect of the morphology of the ice–solution front on the cell volume response. The morphology of the interface can be controlled by varying the surface tension. For a high enough value, such as $\gamma_0 = 1.65$ N/m, interfacial instabilities can be suppressed and the front will then propagate as an unperturbed circle as it approaches the cell. For the case shown in Fig. 3(c), changing the surface tension value does not cause much effect on the volume response curve for the lower cooling rate value (1000 °C/min). In fact, the Gibbs–Thomson effect (Eq. (3)) depresses the interface temperature by only a small value. The morphology of the interface, however, is very sensitive to small changes in the interfacial tension and the wavelengths of the interfacial instabilities depend on this value. In Fig. 2(a)–(d) we showed the interaction of an initially perturbed ice front with a cell when the surface tension of the ice–solution interface is given an artificially high value in order to suppress instabilities. This case may be contrasted with that in Fig. 6 (for the same cooling rate as in Fig. 2), where the surface tension is given the value for pure ice–water interface, and an initial perturbation was imposed as described previously. These two cases illustrate the effects of interfacial tension on cell–ice interaction. The final shape of the ice front is determined by the capillarity effects. While the high surface tension restabilizes the interface in Fig. 2, for the low interfacial tension in Fig. 6, the interface becomes unstable and the salt is segregated in deep grooves between the fingers of ice. The cell in Fig. 2 faces a nearly uniform solute distribution in the extracellular medium, while that in Fig. 6 sees a more inhomogeneous environment. However, for the geometry and conditions investigated here, the Peclet number is small and the solute in the extracellular medium homogenizes rapidly. In both cases the formation of ice and shrinkage of cell occur rapidly (in about 0.7 s, corresponding to a temperature of −12 °C). In Figs. 2(e), (f) and 6(d), (e) we show the profiles of salt concentrations across the domain at the horizontal centerline of the domain. Clearly the solute distribution in the unstable case is different from the stable case since

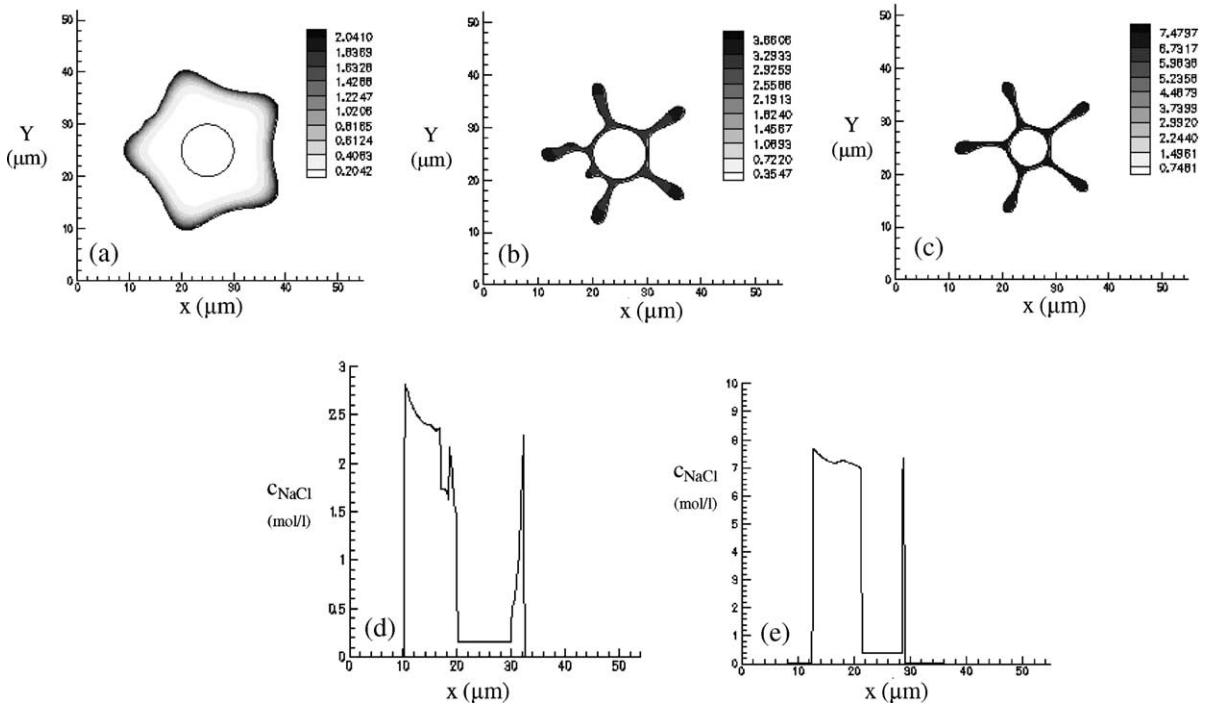

Fig. 4. The interaction of an unstable ice front with the cell. Cooling rate $B = 10{,}000$ °C/min, $T_0 = -5.46$ °C, surface tension = 0.165 N/m. A 250×250 grid was used. Salt concentration contours (gray-scales indicate levels in mol/l) are shown at: (a) $t = 9.215\text{E}{-}03$ s, $T = -6.997$ °C; (b) $t = 3.31339\text{E}{-}02$ s, $T = -10.981$ °C; (c) $t = 0.111$ s, $T = -24.031$ °C. Concentration profile of NaCl across the horizontal centerline of the cell: (d) corresponding to the contours in (b); (e) corresponding to the contours in (c).

the rejected salt accumulates in the grooves between the ice fingers. However, the concentration field in the solution between the ice front and the cell is comparable in the two cases. Therefore, the nature of the interface stability does not appear to have much of an impact on the cell–ice interaction behavior for the particular cases shown in Figs. 2 and 6. In particular, the volumetric response of the cell is almost identical for the two values of the surface tension for the low cooling rate, as shown in Fig. 3(c). For a higher cooling rate (10 000 °C/min) the interfacial instability does affect the volume response of the cell when compared to a stable interface case, as seen in Fig. 3(c). However, the differences for the present configuration are modest. Note however, that this conclusion applies for the particular configuration chosen for simulation in the present case. In general, the response of the cell to the advancing ice front may be more significantly affected by the nature of the interfacial instabilities (such as the tip velocity, and tip curvature) and also by the distance of the ice front from the cell at the onset of cooling. This is because the solute concentration at the tip of the steady-state dendrite (and the distribution of solute in the boundary layer that accompanies the steadily propagating tip) will depend on the thermal conditions (through Eq. (3)). These aspects are being investigated using the present numerical technique in ongoing work.

The effect of varying the membrane permeability on the volumetric response of the cell due to water loss from osmosis is shown in Fig. 7. The permeability value L_p has been varied in 10 equal intervals between the values of 1.66×10^{-12} m/(s Pa) and 1.66×10^{-11} m/(s Pa). The cooling rate here is 1000 °C/min. The lower value of permeability (L_{p0}) corresponds to that of the red blood cell. The volume response of the cell in each case is shown against time. The cell with high permeability shrinks rapidly (in about 0.2 s) while the low permeability cell takes about three times as long to lose all the water. There is clearly a highly non-linear relationship between the permeability and the time of shrinkage. In order to compare our results with those of the membrane-limited (Mazur) model in terms of survival prediction, we plot the temperature at which the cell water volume reaches 5% of its initial value. The predictions from the present calculations are in fair agreement with that obtained from the Mazur model in terms of the trend but the present calculations indicate that the minimum temperature experienced at this level of shrinkage is marginally higher than that indicated by the Mazur model. For the range of permeabilities and

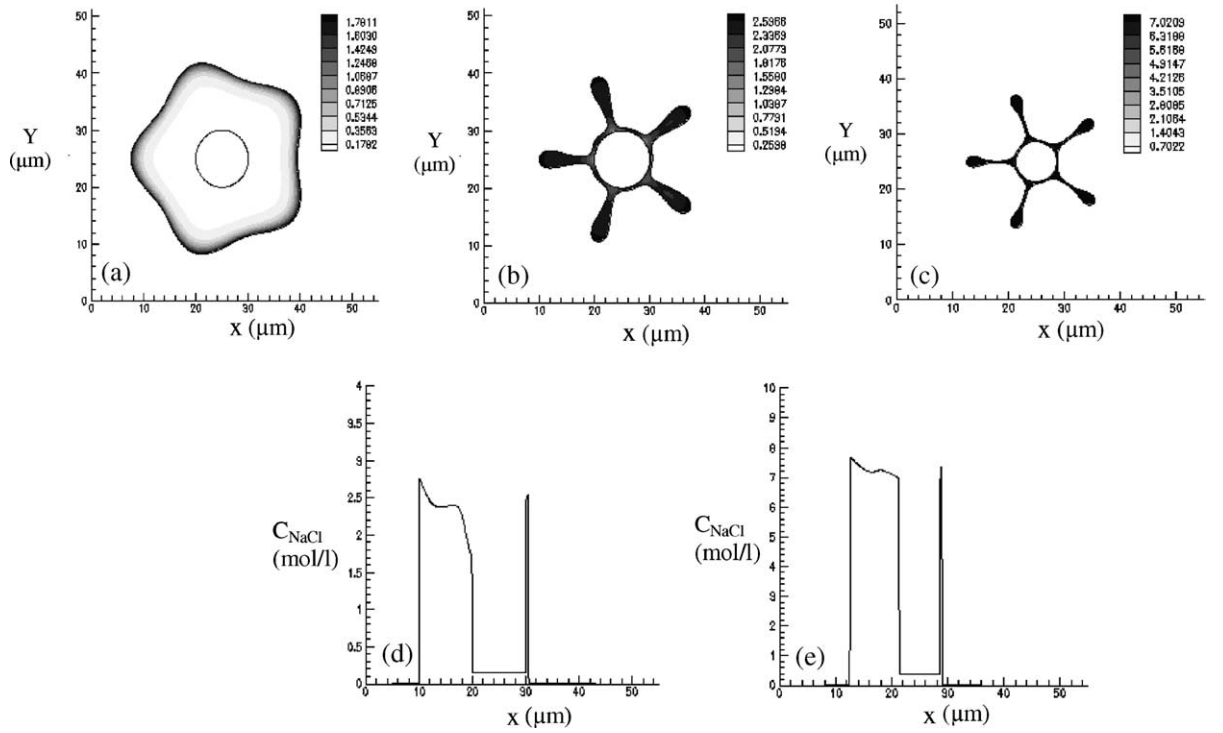

Fig. 5. The interaction of an unstable ice front with the cell. Cooling rate $B = 10{,}000$ °C/min from $T_0 = -5.46$ °C, surface tension = 0.165 N/m. A 500×500 grid was used. Salt concentrations contours (with gray-scales indicating the levels in mol/l) are plotted at: (a) $t = 5.09\text{E}{-}03$ s, $T = -6.3111$ °C; (b) $t = 1.73\text{E}{-}02$ s, $T = -8.3415$ °C; (c) $t = 0.1137$ s, $T = -24.401$ °C. Concentration profile of NaCl across the horizontal centerline of the cell: (d) corresponding to the contours in (b); (e) corresponding to the contours in (c).

cooling rate used here the Peclet numbers remain small and hence the membrane-limited model appears to capture the cell–ice interaction fairly well.

Fig. 8 shows the response of the cell to the extracellular ice formation and compares the result from the present simulations to the Mazur model. The ice formation in each case is initiated as in the above cases, with a circular front 4 cell radii away from the center of the cell. The initial temperature is −0.5 °C in each case. The ice front reaches the cell and begins to interact with it after an interval, so that the temperature at which the interaction begins is different for different cooling rates. To compare with the Mazur model, we computed the volume loss in the Mazur model by starting from the temperature at which the ice and cell begin to interact in our simulations. Fig. 8(a) and (b) show volume loss curves for two values of the cooling rate, 1000 and 5000 °C/min respectively. The volume loss predicted from the present simulations are in close agreement with that of the Mazur model as would be expected for the low Peclet number regime considered in this study. Predictions of the solute fields on the extra- and intracellular membrane surfaces for the present simulations (where the concentrations are averaged over the circumference of the cell) and the membrane-limited Mazur model are made in Fig. 9. Fig. 9(a) shows the intra- and extracellular membrane surface concentrations at the low cooling rate of 1000 °C/min while Fig. 9(b) shows these values for the high cooling rate of 5000 °C/min. For both the low as well as high cooling rate, in Fig. 9(a) and (b) respectively, the concentrations for the two models appear to be in fairly good agreement. The extracellular concentration is in better agreement than the intracellular, but the deviation of the intracellular concentrations are small initially and increases in the later stages of the volume loss. Fig. 9(c) plots the difference in concentration across the membrane (i.e. the driving force) for the two models. As seen from the figure the present model predicts driving forces in good agreement with the Mazur model as indicated by the good agreement of the volume loss curves in Fig. 8.

In Fig. 10, we show the interaction between the cell and ice front when the domain is not maintained at a uniform temperature. The temperature is allowed to vary in the domain and the transport equation for heat is solved in a fully coupled fashion along with the solute transport equation. The boundary condition for temperature, Eq. (5) is applied at the interface. The cooling rate is imposed to obtain the temperature on the edges of the domain. The freezing interface consequently assumes

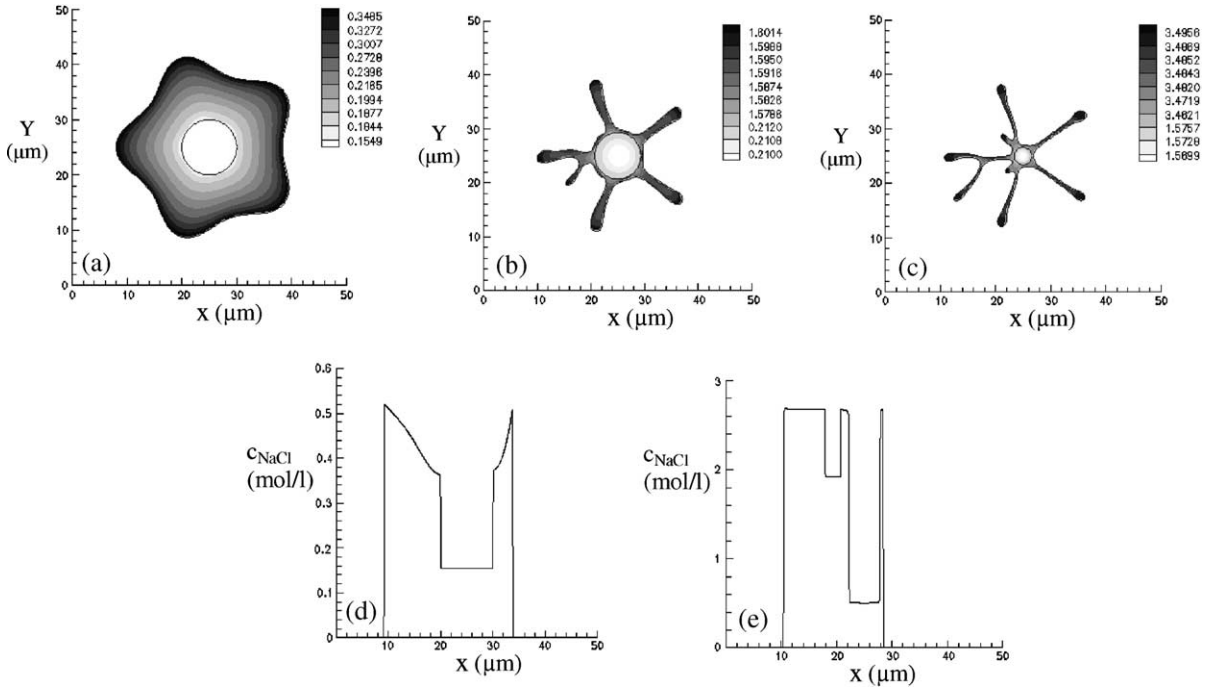

Fig. 6. The interaction of an unstable ice front with the cell. Cooling rate $B = 1000$ °C/min from $T_0 = -0.54$ °C, surface tension = 3.307E−2 N/m. Salt concentrations are shown at: (a) $t = 0.0416$ s, $T = -1.2384$ °C; (b) $t = 0.2894$ s, $T = -5.3664$ °C; (c) $t = 0.6711$ s, $T = -11.722$ °C. Concentration profile of NaCl across the horizontal centerline of the cell for: (d) time corresponding to (a); (e) time corresponding to (b).

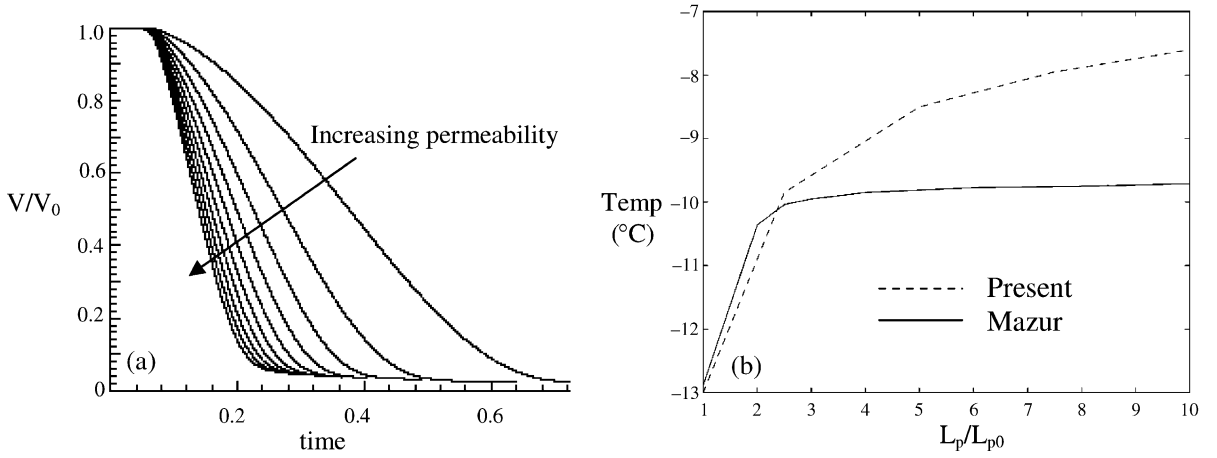

Fig. 7. The response of the cell for a cooling rate of $B = 1000$ °C/min, as the permeability of the cell membrane is varied. (a) The 10 curves correspond to values from 1.66E−12 m/(s Pa) to 1.66E−11 m/(s Pa) in increments of 1.66E−12 m/s Pa. (a) Plot of the volume versus time. (b) Temperature at which cell water volume reaches 5% of the initial value.

a shape that reflects the square shape of the domain up to the stage that the front closes in on the cell. The concentration and temperature contours during the freezing process are shown in Fig. 10. The temperature field is seen to vary across the domain with the domain edges being colder than the center. Solute concentration and temperature profiles are shown in Fig. 10(c) and (d) respectively. The solute field shows large jumps at the cell membrane. The temperature field is continuous everywhere, with discontinuous slope at the ice–liquid

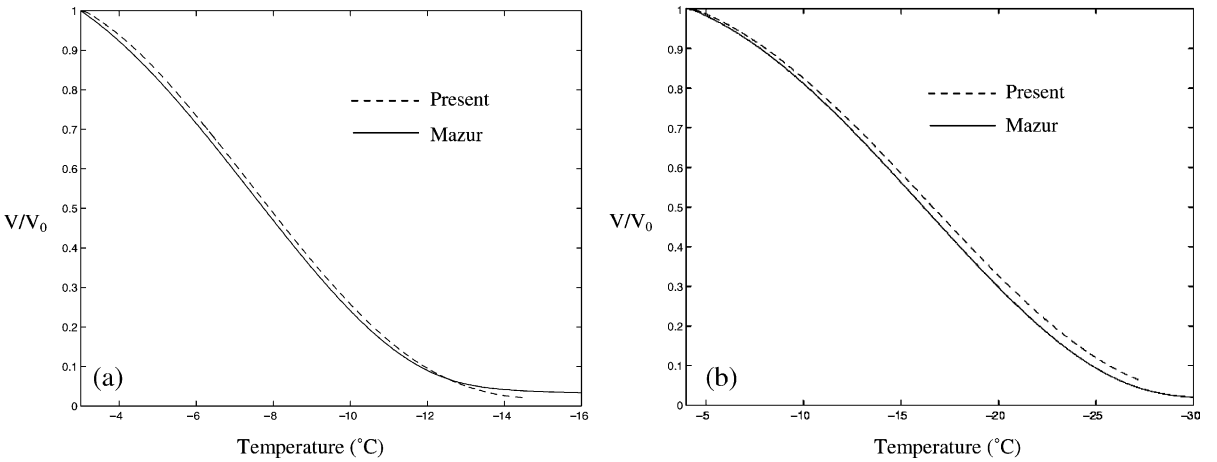

Fig. 8. Response of the cell to extracellular ice. Comparison of simulation results (—) is made with the Mazur model (- - -) for two different cooling rates: (a) $B = 1000$ °C/min, (b) $B = 5000$ °C/min.

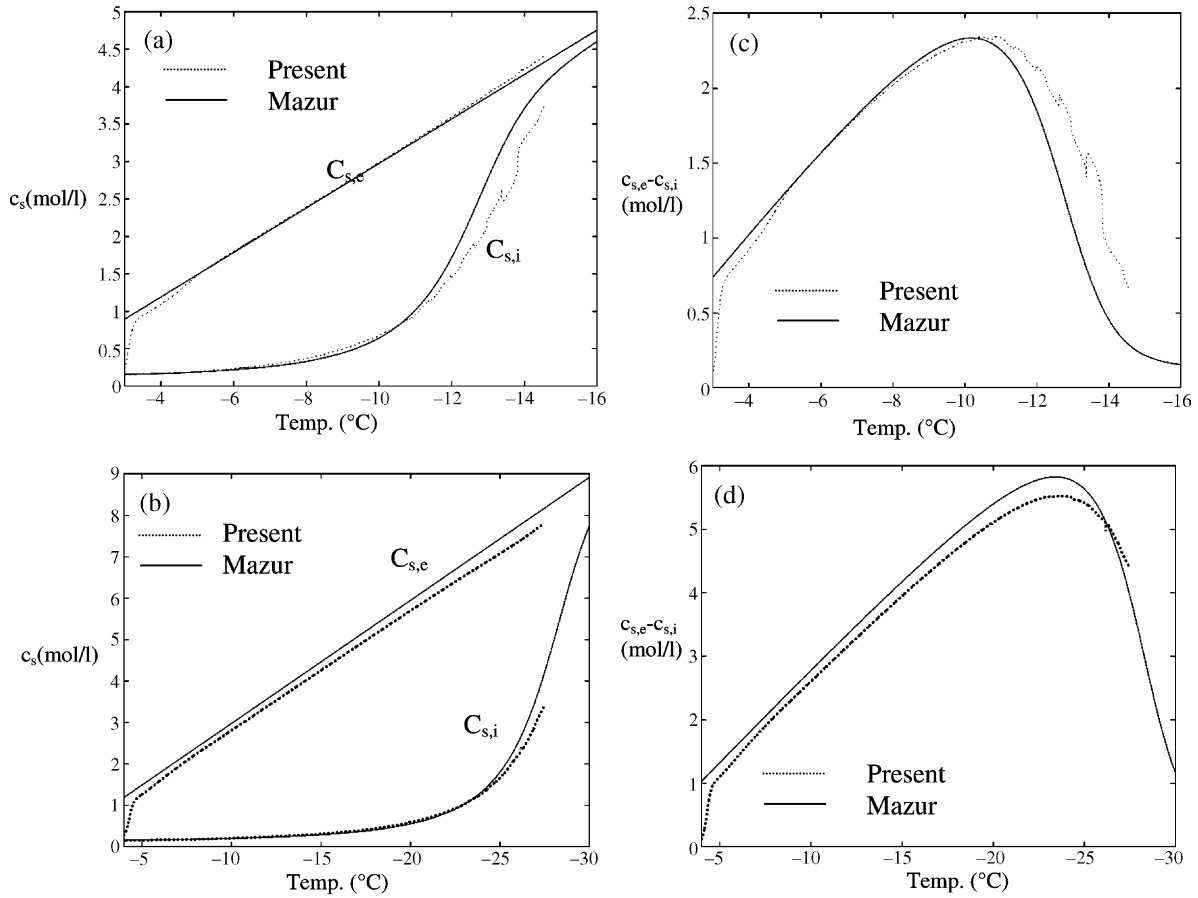

Fig. 9. Comparison of predictions made by the present simulations and the membrane-limited Mazur model. (a) The intra- and extracellular salt concentrations for cooling rate of 1000 °C/min. (b) Intra- and extracellular salt concentrations for cooling rate of 5000 °C/min. (c) Difference between the extra- and intracellular salt concentrations at 1000 °C/min. (d) Difference between the extra- and intracellular salt concentrations at 5000 °C/min.

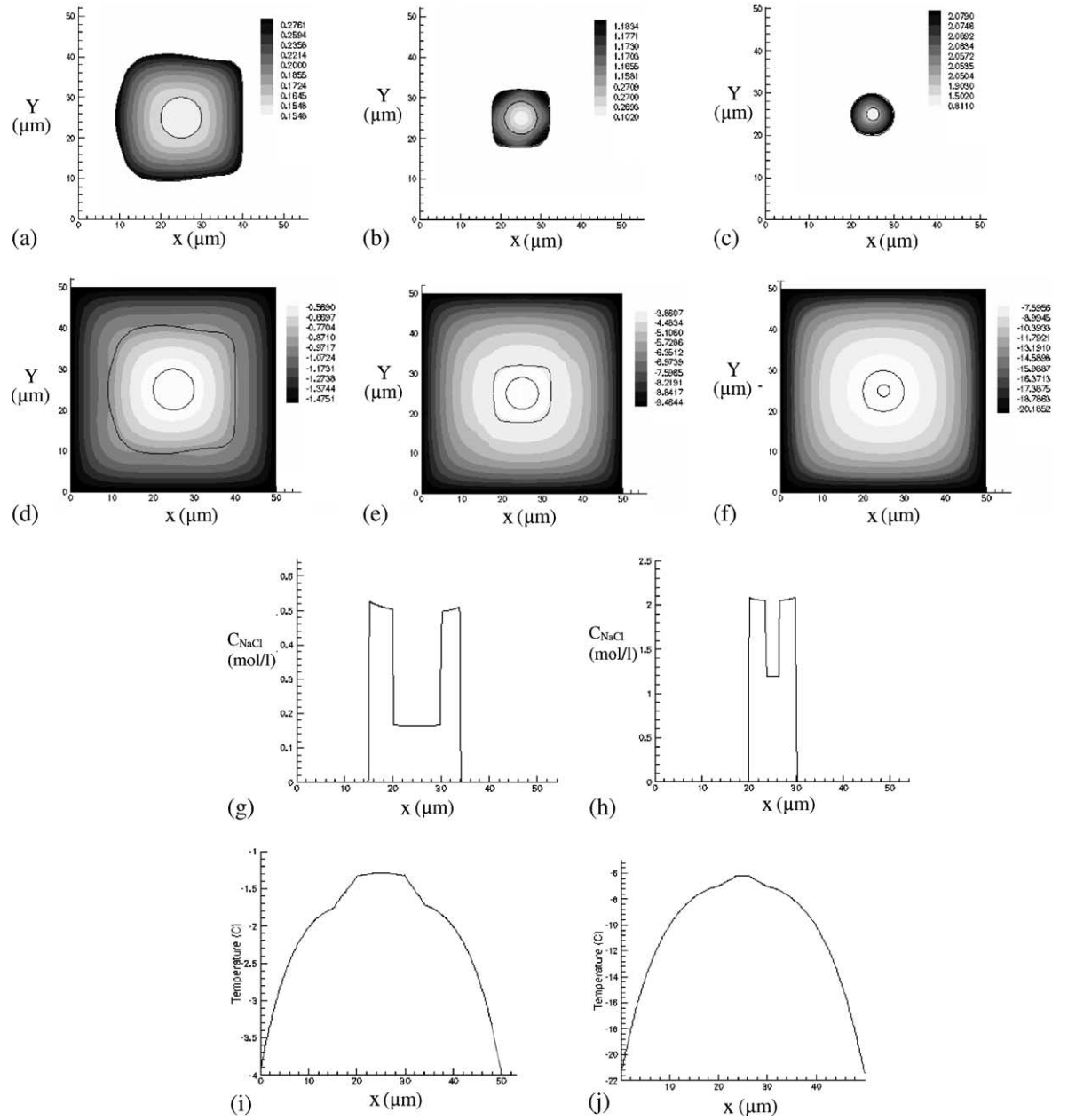

Fig. 10. The interaction of an unstable ice front with the modeled cell under non-isothermal condition. Cooling rate $B = 1000$ °C/min from $T_0 = -0.5$ °C, surface tension = 3.307E−2 N/m. NaCl concentration contours (gray-scale indicates levels in mol/l) at: (a) $t = 0.062$ s, (b) $t = 0.57$ s, (c) $t = 1.26$ s. Temperature contours (gray-scale indicates levels in °C) at: (d) $t = 0.062$ s, (e) $t = 0.57$ s, (f) $t = 1.26$ s. NaCl concentration profiles across the horizontal centerline of the cell at: (g) $t = 0.20$ s, (h) $t = 1.26$ s. Temperature profiles across the horizontal centerline of the cell at: (i) $t = 0.20$ s, (j) $t = 1.26$ s.

interface due to latent heat release and at the membrane due to jump in the salt concentration. The variation of temperature across the domain is small (about 0.6 °C). However, the rate of cell water loss can be significantly different for the non-isothermal case as opposed to the isothermal situation, as demonstrated in Fig. 11. Traditional methods for analyzing volume response of cells have relied on Mazur's [7] original approach where the medium is assumed isothermal (i.e. latent heat effects and the heat transport phenomena are ignored) and the solute polarization in the extra- and intracellular medium is ignored. In Fig. 11 we compare the volumetric

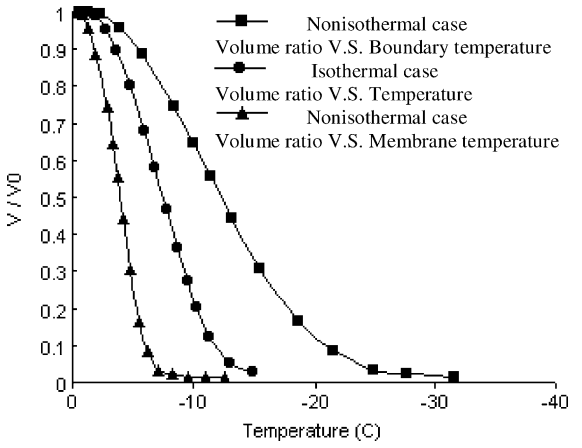

Fig. 11. The volume response of the cell for the isothermal and non-isothermal cases. Cooling rate $B = 1000$ °C/min.

response of the cell against the temperature for the isothermal and non-isothermal cases, all other parameters in the computation remaining identical. Note that since the temperature is decreased at a constant rate in the cooling process, the x-axis in Fig. 11 can also be thought of as the time axis. Clearly, the results from the isothermal and non-isothermal cases differ significantly. Thus, the thermal and solutal inhomogeneities can couple in a non-linear fashion with the temperature-dependent membrane permeability to provide cell volume response that deviates significantly from estimates of such response obtained from the Mazur model. The interface shape, temperature and composition are all fully coupled in the non-isothermal case through the curvature, the Gibbs–Thomson effect and the phase diagram. This coupling causes significant deviation of the freezing behavior and solute rejection at the ice–solution interface and thus the driving force for cell water loss is impacted. Thus, there may be significant differences between the cell response observed in a cryomicroscope (under isothermal conditions) and the actual cell response when cryopreserved in a straw or vial (under non-isothermal conditions). This may in part explain the large discrepancies in predicted and observed optimal cooling rates for sperm cryopreservation [21].

5. Conclusions

Numerical simulations of the interaction of ice with biological cells have been performed to study the response of the cell to ice formation in the extracellular medium. The sharp interface numerical method employed allows for the computation of ice formation and cell shrinkage on a fixed Cartesian mesh. Solute polarization at the ice–liquid interface and the cell membrane has been accounted for in the model. The thermophysical data employed in the paper have been obtained from the literature and correspond to physiological aqueous salt solutions and red blood cells. The effects of various parameters on the response of the cell have been studied. The kinetics of cell dehydration is related in a highly non-linear fashion to the membrane permeability. For the parameters studied in this paper, the results on cell volume loss obtained from the present and Mazur models appear to be in good agreement for a wide range of permeabilities and cooling rates. Thus, for the particular configuration chosen in the present study (i.e. the cell is surrounded on all sides by the ice front, there are no cryoprotectant additives, and the diffusion coefficients are constant) and for the low Peclet number regimes investigated, solute polarization and interfacial morphology appear to have only modest effects on the response of the cell. However, it is found that the assumption of temperature uniformity in the sample can have a significant influence on predictions of cell volume response. Even though the temperature differences are small in the non-isothermal cases studied, there is a significant difference in the response of the cell to ice between the isothermal and non-isothermal situations.

In an upcoming paper the action of cryoprotective agents, which are used in practical cryopreservation protocols, are studied by modeling the transport and solidification processes in ternary systems. In ongoing work the complex dependencies of the cell volume on the various thermophysical parameters and on the processing parameters are being investigated in greater detail. In particular, regimes in which the conventional membrane-limited transport model is known to fail [22] are being explored. The model presented is also being coupled with a model for prediction of intracellular ice formation in order to be able to predict cell survival probabilities.

Acknowledgements

H.S. Udaykumar would like to acknowledge support from the Whitaker Foundation (Biomedical Engineering Research Grant) and the NSF CAREER program (CTS-0092750). J.O.M. Karlsson acknowledges support from the NSF CAREER program (BES-0242377).

Appendix A

The relevant dimensional quantities used in the calculations are as follows: the diameter of the cell $X = 10$ [μm], the time scale for mass transport $t_c = X^2/D_l = 0.1282$ [s] and the initial concentration of the solute $c_0 = 0.1548$ [mol/l].

The material parameters used in the calculations are: thermal diffusivity of liquid (water) $\alpha_l = 0.115$ [mm^2 s^{-1}], thermal diffusivity of solid (ice) $\alpha_s = 1.364$ [mm^2 s^{-1}], binary diffusivity of NaCl in liquid $D_l = 7.8 \times 10^{-4}$ [mm^2 s^{-1}], binary diffusivity of NaCl in solid $D_s = 7.8 \times 10^{-7}$ [mm^2 s^{-1}], latent heat of fusion $L = 0.333$ [J mm^{-3}], equilibrium freezing point $T_m = 273.15$ [K], partition coefficient $p = \frac{(c_{NaCl})_s}{(c_{NaCl})_l} = 1.00 \times 10^{-3}$, thermal conductivity of liquid $k_l = 5.36 \times 10^{-4}$ [J mm^{-1} s^{-1} K^{-1}], thermal conductivity of solid (ice) $k_s = 2.34 \times 10^{-3}$ [J mm^{-1} s^{-1} K^{-1}]. The permeability $L_{p0} = 1.66 \times 10^{-12}$ m/s Pa, and surface tension $\gamma_0 = 0.033$ N/m. The liquidus curve is given by $T_{Li} = b_0 + b_1 c_{Li} + b_2 c_{Li}^2 + b_3 c_{Li}^3 + b_4 c_{Li}^4$ where $b_0 = 273.15$ [K], $b_1 = -3.362$ [K l mol^{-1}], $b_2 = -0.0414$ [K l^2 mol^{-2}], $b_3 = -0.0404$ [K l^3 mol^{-3}], $b_4 = -6.616 \times 10^{-4}$ [K l^4 mol^{-4}].

References

[1] K.R. Diller, Intracellular freezing: effect of extra-cellular supercooling, Cryobiology 12 (1975) 480–485.

[2] J.E. Lovelock, Haemolysis of human red blood cells by freezing and thawing, Biochim. Biophys. Acta 10 (1953) 414–426.

[3] P. Mazur, K.W. Cole, Roles of unfrozen fraction, salt concentration and changes in cell volume in the survival of frozen human erythrocytes, Cryobiology 26 (1989) 1–29.

[4] D.E. Pegg, M.P. Diaper, An unfrozen fraction hypothesis of freezing injury to human erythrocytes: a critical examination of the evidence, Cryobiology 26 (1989) 30–43.

[5] H.T. Meryman, Osmotic stress as a mechanism of freezing injury, Cryobiology 8 (1971) 489–500.

[6] P.L. Steponkus, W.J. Gordon-Kamm, Cryoinjury of isolated protoplasts: a consequence of dehydration or the fraction of suspended medium that is frozen, Cryo-Lett. 6 (1985) 217–226.

[7] P. Mazur, Kinetics of water loss from cells at subzero temperatures and the likelihood of intracellular freezing, J. Gen. Physiol. 47 (1963) 347–369.

[8] M. Toner, Nucleation of ice crystals inside biological cells, in: P. Steponkus (Ed.), Advances in Low-Temperature Biology, vol. 2, JAI Press, London, 1993, pp. 1–51.

[9] P. Mazur, The role of intracellular freezing in the death of cells cooled at supra-optimal rates, Cryobiology 14 (1977) 251–272.

[10] M. Toner, E.G. Cravalho, M. Karel, Thermodynamics and kinetics of intracellular ice formation during freezing of biological cells, J. Appl. Phys. 67 (3) (1990) 1582–1593.

[11] R.L. Levin, E.G. Cravalho, C.G. Huggins, Diffusion in a liquid solution with a moving semi-permeable boundary, J. Heat Transfer, Trans. ASME 99 (1977) 322–329.

[12] R.L. Levin, E.G. Cravalho, C.G. Huggins, The concentration polarization effect in frozen erythrocytes, J. Biomech. Eng., Trans. ASME 99 (1977) 65–73.

[13] R.L. Levin, The freezing of finite domain aqueous solutions: solute redistribution, Int. J. Heat Mass Transfer 24 (9) (1981) 1443–1455.

[14] H.S. Udaykumar, R. Mittal, W. Shyy, Computation of solid–liquid phase fronts in the sharp interface limit on fixed grids, J. Comput. Phys. 153 (1999) 535–574.

[15] H.S. Udaykumar, L. Mao, R. Mittal, A finite-volume sharp interface scheme for dendritic growth simulations: comparison with microscopic solvability theory, Numer. Heat Transfer B 42 (5) (2002) 389–409.

[16] H.S. Udaykumar, L. Mao, Sharp-interface simulation of dendritic solidification of solutions, Int. J. Heat Mass Transfer 45 (2002) 4793–4808.

[17] M. Jaeger, M. Carin, M. Medale, G. Tryggvason, The osmotic migration of cells in a solute gradient, Biophys. J. 77 (1999) 1257–1267.

[18] M. Jaeger, M. Carin, The front-tracking ALE method: application to a model of the freezing of cell suspensions, J. Comput. Phys. 179 (2002) 704–735.

[19] K. Wollhöver, Ch. Körber, M.W. Scheiwe, U. Hartmann, Unidirectional freezing of binary aqueous solutions: an analysis of transient diffusion of heat and mass, Int. J. Heat Mass Transfer 28 (1985) 761–769.

[20] G.B. McFadden, A.A. Wheeler, R.J. Braun, S.R. Coriell, Phase-field models for anisotropic interfaces, Phys. Rev. E 48 (3) (1993) 2016–2024.

[21] M.R. Curry, J.D. Millar, P.F. Watson, Calculated optimal cooling rates for ram and human sperm cryopreservation fail to conform with empirical observations, Biol. Reprod. 51 (1994) 1014–1021.

[22] A.V. Kasharin, J.O.M. Karlsson, Analysis of mass transport during warming of cryopreserved cells, Ann. New York Acad. Sci. 858 (1998) 160–171.